Ultrasound-triggered piezocatalytic composite hydrogels for promoting bacterial-infected wound healing

Dun Liu [a,1], Lei Li [b,1], Ben-Long Shi [a,1], Bo Shi [a], Ming-Ding Li [b], Yong Qiu [a], Di Zhao [c,***], Qun-Dong Shen [b,**], Ze-Zhang Zhu [a,*]

[a] Division of Spine Surgery, Department of Orthopedic Surgery, Affiliated Drum Tower Hospital, Medical School of Nanjing University, Nanjing, 210008, China
[b] Department of Polymer Science and Engineering, Key Laboratory of High-Performance Polymer Materials and Technology of MOE, School of Chemistry and Chemical Engineering, Nanjing University, Nanjing, 210023, China
[c] Institute of Brain Science and Disease, School of Basic Medicine, Qingdao University, Qingdao, Shandong, 266001, China

ARTICLE INFO

ABSTRACT

Wound healing has become one of the basic issues faced by the medical community because of the susceptibility of skin wounds to bacterial infection. As such, it is highly desired to design a nanocomposite hydrogel with excellent antibacterial activity to achieve high wound closure effectiveness. Here, based on ultrasound-triggered piezocatalytic therapy, a multifunctional hydrogel is designed to promote bacteria-infected wound healing. Under ultrasonic vibration, the surface of barium titanate ($BaTiO_3$, BT) nanoparticles embedded in the hydrogel rapidly generate reactive oxygen species (ROS) owing to the established strong built-in electric field, endowing the hydrogel with superior antibacterial efficacy. This modality shows intriguing advantages over conventional photodynamic therapy, such as prominent soft tissue penetration ability and the avoidance of serious skin phototoxicity after systemic administration of photosensitizers. Moreover, the hydrogel based on N-[tris (hydroxymethyl)methyl]acrylamide (THM), N-(3-aminopropyl)methacrylamide hydrochloride (APMH) and oxidized hyaluronic acid (OHA) exhibits outstanding self-healing and bioadhesive properties able to accelerate full-thickness skin wound healing. Notably, compared with the widely reported mussel-inspired adhesive hydrogels, OHA/THM-APMH hydrogel due to the multiple hydrogen bonds from unique tri-hydroxyl structure overcomes the shortage that catechol groups are easily oxidized, giving it long-term and repeatable adhesion performance. Importantly, this hybrid hydrogel confines BT nanoparticles to wound area and locally induced piezoelectric catalysis under ultrasound to eradicate bacteria, markedly improving the therapeutic biosafety and exhibits great potential for harmless treatment of bacteria-infected tissues.

1. Introduction

As the first protective barrier between human body and external environment, skin plays a vital role in preventing us from microbial invasion [1,2]. When its integrity and biofunction are disturbed after burns, traffic accidents, or other severe injuries, there is a high probability of chronic wound caused by infection, which has become a heavy burden to patients and public medical system [3–5]. In response to this issue, a series of antibacterial agents were incorporated into wound dressings to give them bactericidal ability [6,7]. Although these antibiotics encapsulated in dressings are usually able to effectively defend bacterial infections, there are still some unavoidable shortcomings, such as uncontrollable drug release, normal cell toxicity, and the most troublesome drug resistance caused by overuse of antibiotics [8]. Therefore,

---

it is imperative to formulate a comprehensive strategy that can treat bacterial infection while facilitating chronic wound repair.

Sonodynamic therapy (SDT), generating highly toxic reactive oxygen species (ROS) by triggering sonosensitizers with exogenous ultrasound (US), has recently emerged as a promising strategy in antibacterial and antitumor fields [9,10]. Sun et al. [11] reported a nano-enzyme enhanced sonodynamic treatment strategy for multidrug resistant bacterial infections and achieved eradication of methicillin-resistant staphylococcus aureus (MRSA). SDT has broadened the way to treat drug-resistant bacteria due to its good biocompatibility and excellent antibacterial properties [12]. Compared to conventional photodynamic therapy (PDT), another non-invasive treatment strategy, SDT shows greater soft tissue penetration ability and avoids serious skin phototoxicity after systemic administration of photosensitizers [13]. During the SDT process, the sonosensitizers instantly produce a large amount of ROS under US irradiation, which have excellent bacteria-killing ability and can significantly reduce the possibility of drug-resistant bacteria. Barium titanate (BaTiO$_3$, BT), a classical wide-bandgap ferroelectric semiconductor, can immediately generate built-in electric field and surface potential when subjected to external mechanical stress, thereby initiating a redox reaction to generate ROS [14,15]. The above-depicted physical phenomenon of transformation between mechanical energy and electrical energy mediated by stress-induced deformation of piezoelectric materials is called piezoelectric effect, which inspires us that BT nanoparticles might be applied as a high-efficient sonosensitizer for sonodynamic antibacterial therapy.

Besides high-efficiency antibacterial ability, suitable microenvironment is essential for bacteria-infected wound regeneration. Hydrogels attract increasing attentions, as they can provide a moist environment, remove excess wound exudate, and prevent bacteria invasion [16–18]. However, the shape of wound is usually irregular, leading to a dilemma that part of the wound will be exposed when treated with traditional hydrogels. Hence, injectable hydrogels are widely accepted as the most attractive wound dressing with shape adaptability. Nevertheless, the majority of existing hydrogel dressings with the above characteristic tend to be deformed or damaged under external force due to poor mechanical elasticity [19,20]. Thus, endowing injectable wound hydrogel dressings with rapid self-healing capability is an urgent to maintain the scaffold structural stability after external damage. Furthermore, adhesion and retention of biomaterials at the wound site are vital factors in skin tissue repair [21,22]. Previous works have also clearly demonstrated the great potential of adhesive hydrogels in wound regeneration, and the most reported adhesive hydrogels involve mussel-inspired catechol functional groups [23–25]. However, the catechol groups are susceptible to be oxidized by oxygen in air to quinone groups, which may limit their long-term and repeatable adhesion properties. In order to address this problem, a new adhesive hydrogel with high density of hydrogen bond (H-bond) was designed. N-[tris(hydroxymethyl)methyl] acrylamide (THM), due to its unique tri-hydroxyl structure, was chosen to be the principal component of the strong bioadhesive hydrogel dressing. N-(3-aminopropyl)methacrylamide hydrochloride (APMH) was grafted to THM to promote chemical crosslink [26]. Additionally, hyaluronic acid (HA), a key ingredient of the extracellular matrix, as well as its oxidized form, oxidized hyaluronic acid (OHA), has shown a wide range of applications in tissue engineering and other biomedical fields in the result of their advantage of non-toxic and non-immunogenic [27,28]. The dynamic Schiff-base covalent bonds between OHA and THM-APMH confer the hydrogels with rapid autonomous healing ability and prolonged lifespan to maintain the structural stability [29–31]. Meanwhile, multiple H-bonds from tri-hydroxyl structure increase the interfacial toughness, giving the OHA/THM-APMH hydrogel excellent tissue adhesion even without any chemical reaction.

In this work, ultrasound and piezocatalytic chemistry are creatively combined via BT nanoparticles for effective bacteria killing through ROS generation under US stimulation, which is named here US-triggered piezocatalytic therapy. On this ground, a composite injectable hydrogel dressing characterized with soft mechanical properties similar to extracellular matrix, significant bactericidal ability and strong adhesiveness, as well as good self-healing properties was developed to accelerate infected cutaneous wound repair (Fig. 1). With the synergistic effect of US-triggered piezocatalytic therapy, the multifunctional hydrogel dressing exhibited excellent antibacterial properties *in vitro* and *in vivo*, while simultaneously enhancing bacterial-infected wound repair by promoting epithelial cell migration, alleviating inflammation, and accelerating angiogenesis. Notably, the adhesive hydrogel confined BT nanoparticles to the wound area and locally induced piezocatalytic bacterial eradication under US irradiation, which minimized the side effects. It should be emphasized that, due to the prominent soft tissue penetration ability of US, our study provides a proof of principle in remote treatment of deep intractable infection (such as deep intramuscular abscess, paravertebral infection, and even gastrointestinal infection), rather than being limited to the treatment of superficial infected wounds. To the best of our knowledge, this is the first time to report a comprehensive strategy combining US and piezoelectric nanoparticles-embedded multifunctional hydrogels to treat bacterial-infected wounds. This study will bring about a new perspective on design of wound dressing materials with multiple biofunctions for the treatment of bacterial-infected wounds, especially internal infections that cannot be covered by traditional methods.

2. Results and discussion

2.1. Fabrication and characterization of the composite hydrogel

Ferroelectric BT nanoparticles exhibit great application potential in drug delivery, cell differentiation induction, and tissue regeneration due to its good biocompatibility, good electro-mechanical conversion, and high piezoelectric coefficient [32]. We firstly synthesized BT by a hydrothermal method and obtained noncentrosymmetric tetragonal BT with piezoelectric effect through simple thermal annealing [33]. From the scanning electron microscope (SEM) images, BT nanoparticle has approximately cubic shape with smooth surface (Fig. 2a and b). According to the measurement of dynamic light scattering, the average size of BT nanoparticle was 117 ± 42 nm (Fig. S1a). X-ray diffraction (XRD) patterns confirmed that all diffraction peaks can be well indexed to the perovskite structure of BT (JCPDS, No. 05–0626) (Fig. 2c). The splitting peak at 2θ of 45° was specified as the (002) and (200) planes of the tetragonal phase of BT, demonstrating the piezoelectric properties of BT nanoparticles. Furthermore, the piezoelectricity of BT nanoparticles was directly measured by piezo-response force microscopy (PFM). A typical butterfly-shaped amplitude loop was observed, verifying the excellent piezoelectric response of the BT nanoparticles (Fig. S1b). As shown in the piezoelectric phase chart (Fig. S1c), there was a about 180° phase switching in the localized piezoelectric hysteresis loop of BT, which further confirmed its piezoelectric performance.

To fabricate a dynamic-bond cross-linked bioadhesive self-healing hydrogel with excellent antibacterial capacity and good adhesiveness, THM-APMA and OHA were synthesized and examined by ^{1}H NMR and Fourier transform infrared (FTIR) spectra. Firstly, THM-APMH was prepared by copolymerized THM with APMH to facilitate crosslinking. The characteristic peak of THM-APMH at 3.7 ppm (methylene of THM monomer compared with Fig. S2a) [34,35] and those at 2.1, 2.9, and 3.2 ppm (methylene) of APMH were observed (Fig. 2d). The FTIR spectra of HA and OHA were very similar, while a weak signal at 1729 cm^{-1} of OHA was detected (Fig. S2b), which may be due to the formation of hemiacetals. Meanwhile, two new peaks at 4.9 and 5.0 ppm were observed on the ^{1}H NMR spectrum of OHA (Fig. S2c). This may correspond to hemiacetalic protons formed from the aldehyde groups and neighboring hydroxyl groups. Then, the multifunctional hydrogel was fabricated by the mixing of OHA and THM-APMH through Schiff-base bond and H-bond (Fig. 2e), and the hydrogel could be prepared with different concentrations of THM-APMH (Table S1).
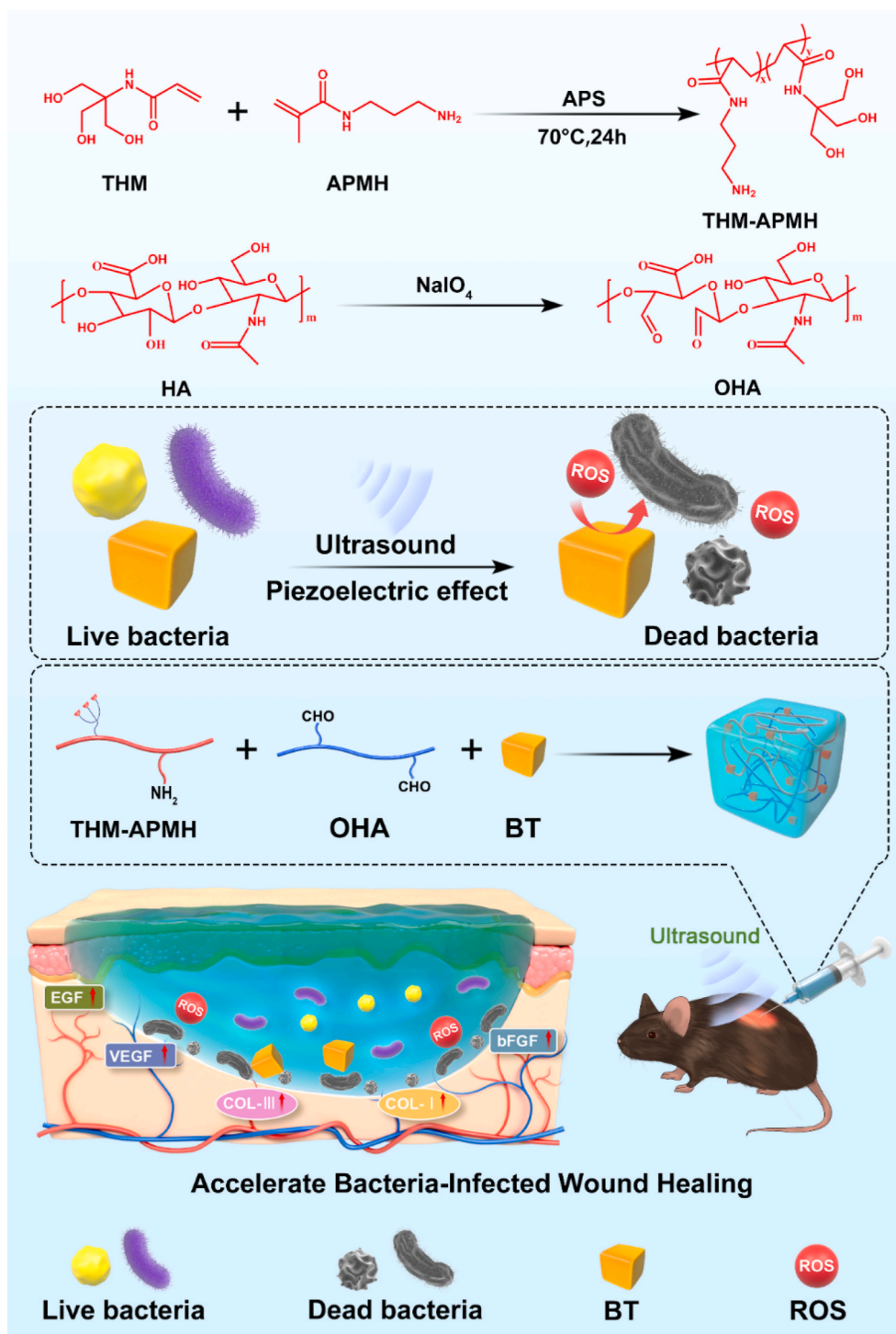
Fig. 1. Schematic illustration of BT-OHA/THM-APMH hydrogel preparation and its synergistic effect with US-triggered piezocatalytic therapy in repairing infected wounds.

SEM was employed to observe the morphology of OHA/THM-APMH hydrogels (Gel). It was found that the hydrogels prepared had a porous structure (Fig. 2f), and the average pore sizes of OHA/THM-APMH$_{15}$ (Gel$_{15}$), OHA/THM-APMH$_{12}$ (Gel$_{12}$), OHA/THM-APMH$_9$ (Gel$_9$), and OHA/THM-APMH$_6$ (Gel$_6$) were 93, 112, 130, and 148 μm, respectively (Fig. 2g). The variation in pore size may be attributed to the increase of crosslinking density in the network. The injectable multifunctional BT-OHA/THM-APMH (BT-Gel) was prepared by adding BT nanoparticles into the hydrogel. SEM images showed that BT-Gel also has irregular porous knot and internal frame, and a large number of BT nanoparticles

were embedded in the interconnect pore wall of the hydrogel (Fig. S2d).

2.2. Rheological performance and swelling ratio

Structures of hydrogel network are directly related to their mechanical properties. The storage modulus (G′) and loss modulus (G″) of the hydrogels versus time was undertaken on a rheometer. With the increase of THM-APMH content, the G′ value also increased, indicating that Schiff base dynamic covalent bond and multiple H-bond could enhance the mechanical properties of the hydrogel (Fig. 2h).
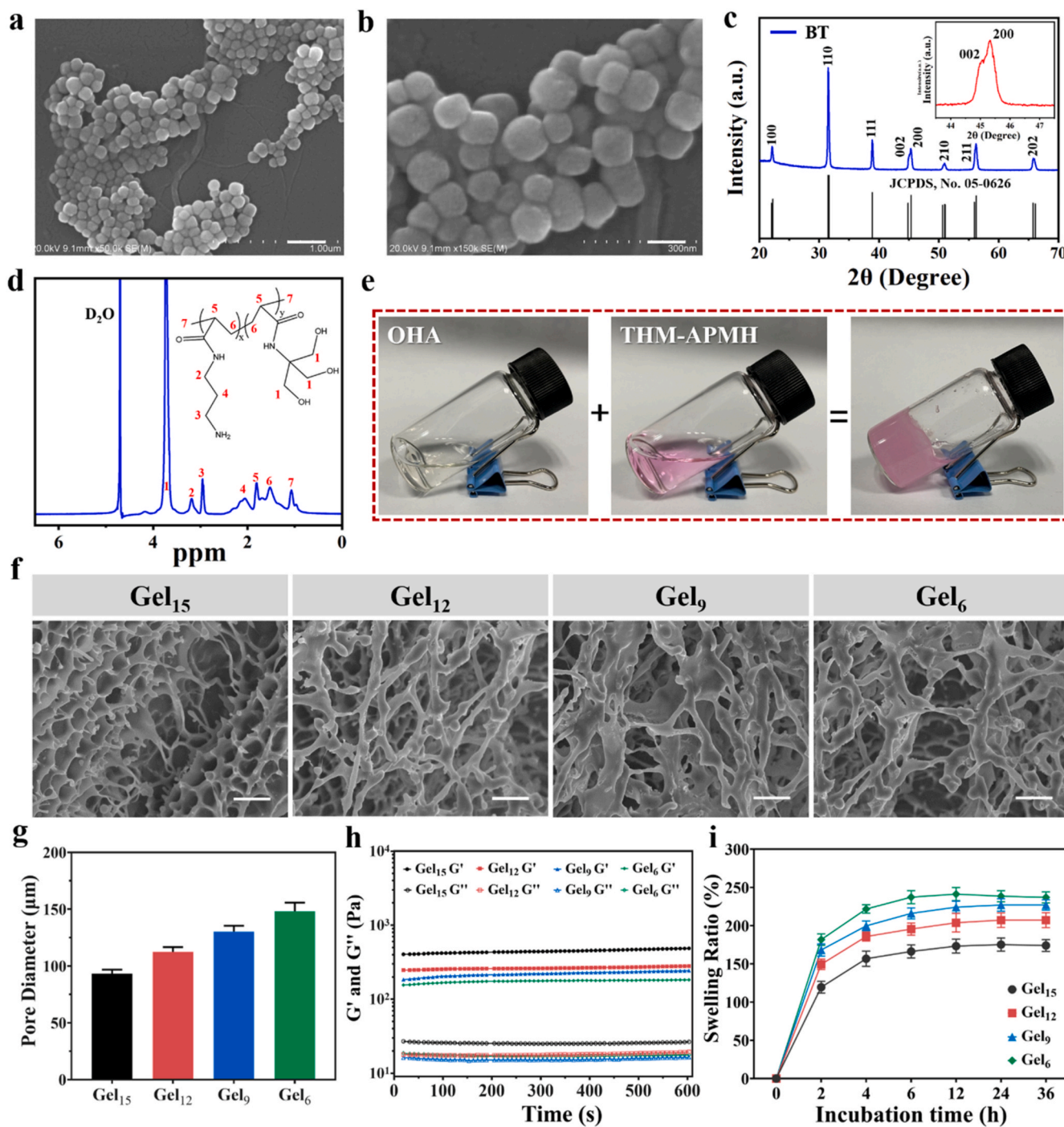
Fig. 2. **Characterization of the prepared BT-Gel. (a–b) SEM images of the BT nanoparticles at varied magnifications.** (a) Scale bar: 300 nm (b) Scale bar: 100 nm. (c) XRD patterns of the BT nanoparticles. (d) ^{1}H NMR spectra of the THM-APMH. (e) Photographs of OHA solution, THM-APMH solution, and the crosslinked hydrogel. (f) SEM images of the hydrogels with different THM-APMH concentration. Scale bars: 100 μm. (g) Pore diameter of the hydrogels. (h) Rheological behavior of the hydrogels. (i) Swelling ratios of the bioadhesive hydrogels.

As desirable wound dressings, multifunctional hydrogels should be able to absorb tissue exudate and maintain a moist microenvironment, which is conducive to wound repair. Therefore, the swelling capacities of above hydrogels were investigated in phosphate buffer saline (PBS) buffer at 37 °C. As shown in Fig. 2i, swelling rates of the hydrogels all increased with the incubation time, and reached an equilibrium swelling state after about 6 h. The swelling ratio of Gel_{15} was 166%, appreciably lower than those of Gel_{12}, Gel_9, and Gel_6. It may be attributed to the increased density of cross-linking network, which was consistent with the hydrogel pore size and storage modulus results. The higher the

crosslinking density, the lower the flexibility and the smaller the swelling tendency of hydrogels. Nevertheless, we hold that the swelling rate of Gel_{15} hydrogel is still high enough to effectively absorb the wound exudate.

2.3. ROS generation ability of BT/BT-Gel with US irradiation

US could trigger the mechanical deformation and subsequent piezoelectric effect of BT nanoparticles. Under US stimuli, a strong built-in electric field were established on the surface of non-centrosymmetric

BT crystal, which could effectively catalyze the generation of ROS through piezoelectric separated electrons and holes on the opposite sides of BT nanoparticles [36] (Fig. 3a). In order to confirm the piezoelectric catalytic effect triggered by US, the degradation of Rhodamine B after different time of US irradiation was investigated (Fig. 3b–3d). In the control group, only slight degradation of Rhodamine B was detected after 10 min of US irradiation (Fig. 3b). In the presence of BT nanoparticles, the absorption at 525 nm decreased gradually with the increase of US irradiation time, indicating that ROS produced by piezoelectric catalysis was US dose-dependent (Fig. 3c). In addition, as expected, BT-Gel and BT nanoparticles had similar ROS generation efficiency with US stimulation, indicating that the multifunctional hydrogel does not weaken its piezoelectric catalytic effect (Fig. 3d). The piezoelectric catalytic performance depended on the piezoelectric power generation efficiency under US [37,38], so the piezoelectric catalytic efficiency was usually used to indirectly reflect the power generation. Hence, we evaluated the piezoelectric catalytic performance of BT and BT-Gel by the curve of relative Rh B concentration ratio C/C0 versus vibration time, where C and C0 were the residual and initial concentrations of Rh B solution (Fig. S3). The result demonstrated that both BT nanoparticles and BT-Gel exhibited powerful piezoelectric catalytic performance with US irradiation. Furthermore, the specific reactive oxygen species generated to degrade Rhodamine B in US-triggered piezoelectric catalysis were verified by electron spin resonance (ESR) technique using 5,5-dimethyl-1-pyrroline-N-oxide (DMPO) to capture unstable radicals. Characteristic signal of DMPO-$\bullet O^{2-}$ and DMPO-$\bullet OH$ were observed in BT nanoparticles, which was consistent with the results of dye degradation experiment (Fig. 3e and f).

2.4. In vitro antibacterial capacity

ROS have excellent bactericidal property by the polyunsaturated phospholipid peroxidation in lipid membrane, and thereby disrupt the selective permeability of bacterial membranes to destroy bacteria [39–43]. To analyze the activity of ROS generated by BT-Gel under US exposure, antibacterial experiments were performed *in vitro* using the spread plate method, bacterial proteins leakage assessment, and bacterial dead/live staining test. *E. coli* and *S. aureus* were selected as representatives of Gram-negative and Gram-positive bacteria, respectively. The bactericidal performance of the different samples was illustrated in Fig. 4. Compared with the groups without US irradiation, it was clearly noted that the bacteria survival rate of the groups under US irradiation was lower both for *E. coli* and *S. aureus* (Fig. 4a and b). The mechanical damage of US and its inertial acoustic cavitation effects were considered as the potential mechanism of the slight bactericidal ability of mere US group and Gel + US group [44]. In the group of BT-Gel with US irradiation, the bactericidal effect was significant improved, and there was almost no bacterial colony formation on the agar plate after US stimulation for 10 min. In addition, the efficacy of US-triggered piezoelectric antibacterial therapy was time-dependent (Fig. 4c and d and S4). With increase of US irradiation time in the existence of BT-Gel, the corresponding bacteria survival rate showed a sharp decrease. For Gram-negative *E. coli*, the bacterial survival rate with BT-Gel under US irradiation for 2 min was 61.0%, while it dramatically decreased to only 0.9% when the US irradiation duration was prolonged to 10 min. Similar results were observed in Gram-positive bacteria (*S. aureus*), demonstrating that the US-triggered piezoelectric effect of BT nanoparticles loaded in hydrogels resulted in the generation of considerable toxic ROS, thus potently enhancing its antibacterial capacity.

The quantitative analysis of bacterial protein leakage was consistent with the bacterial survival rate. In the group of BT-Gel + US, with the longer US irradiation time, the permeability of bacterial cell membrane was damaged more seriously, and the amount of bacterial protein leakage increased accordingly (Fig. 4e and f). Moreover, the fluorescent images of bacteria live/dead staining assay were basically consistent with the above results of spread plate method. In general, the bacteria reduction rate in the groups exposed to US was relatively higher than
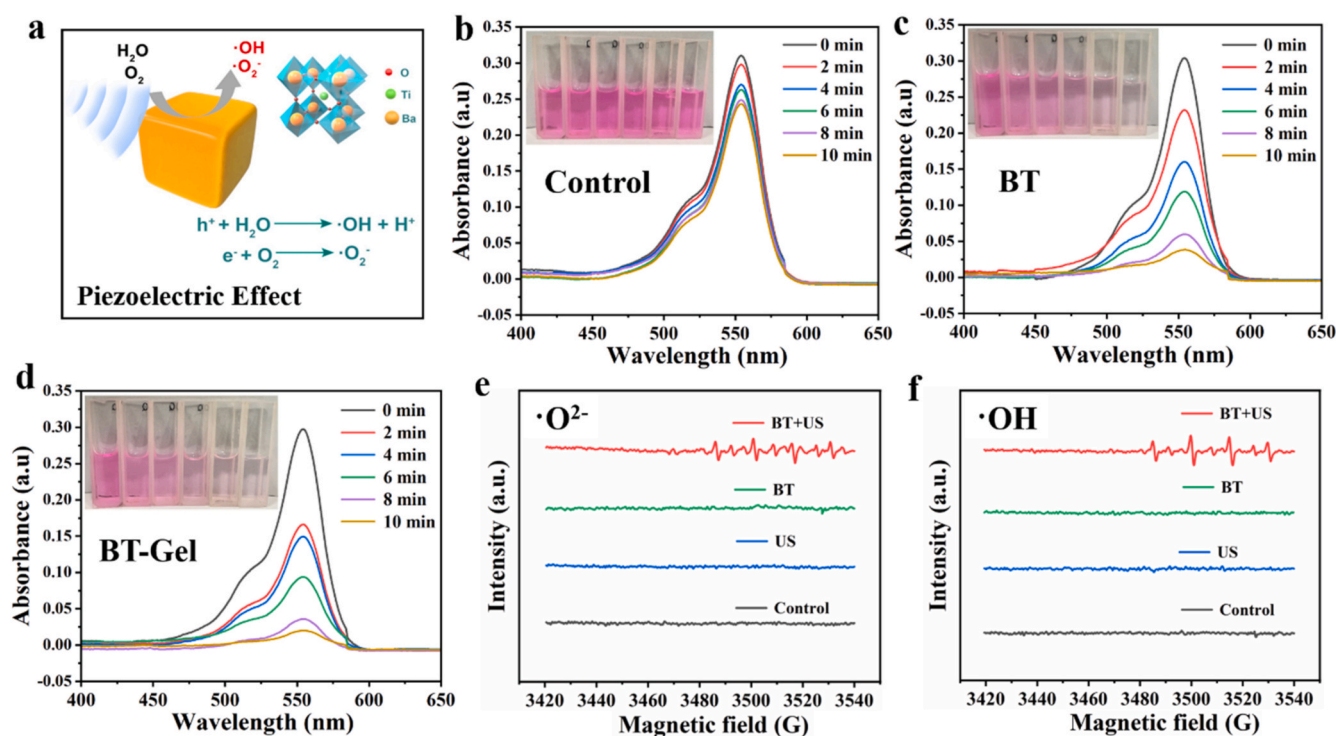

Fig. 3. Piezocatalytic performance of BT/BT-Gel under US irradiation. (a) Schematic illustration of the generation of $\bullet OH$ and $\bullet O^{2-}$ catalyzed by US-triggered BT-mediated piezoelectric effect. UV–Vis absorption spectra of Rhodamine B solution in (b) control, (c) BT nanoparticles, and (d) BT-Gel after different time of US stimulation. Inset pictures from left to right show Rhodamine B solution after different times of US-triggered piezoelectric catalysis. Electron spin resonance spectra of 5,5-dimethyl-1-pyrroline-N-oxide (DMPO) for detecting (e) $\bullet O^{2-}$ and (f) $\bullet OH$ signals in each group.
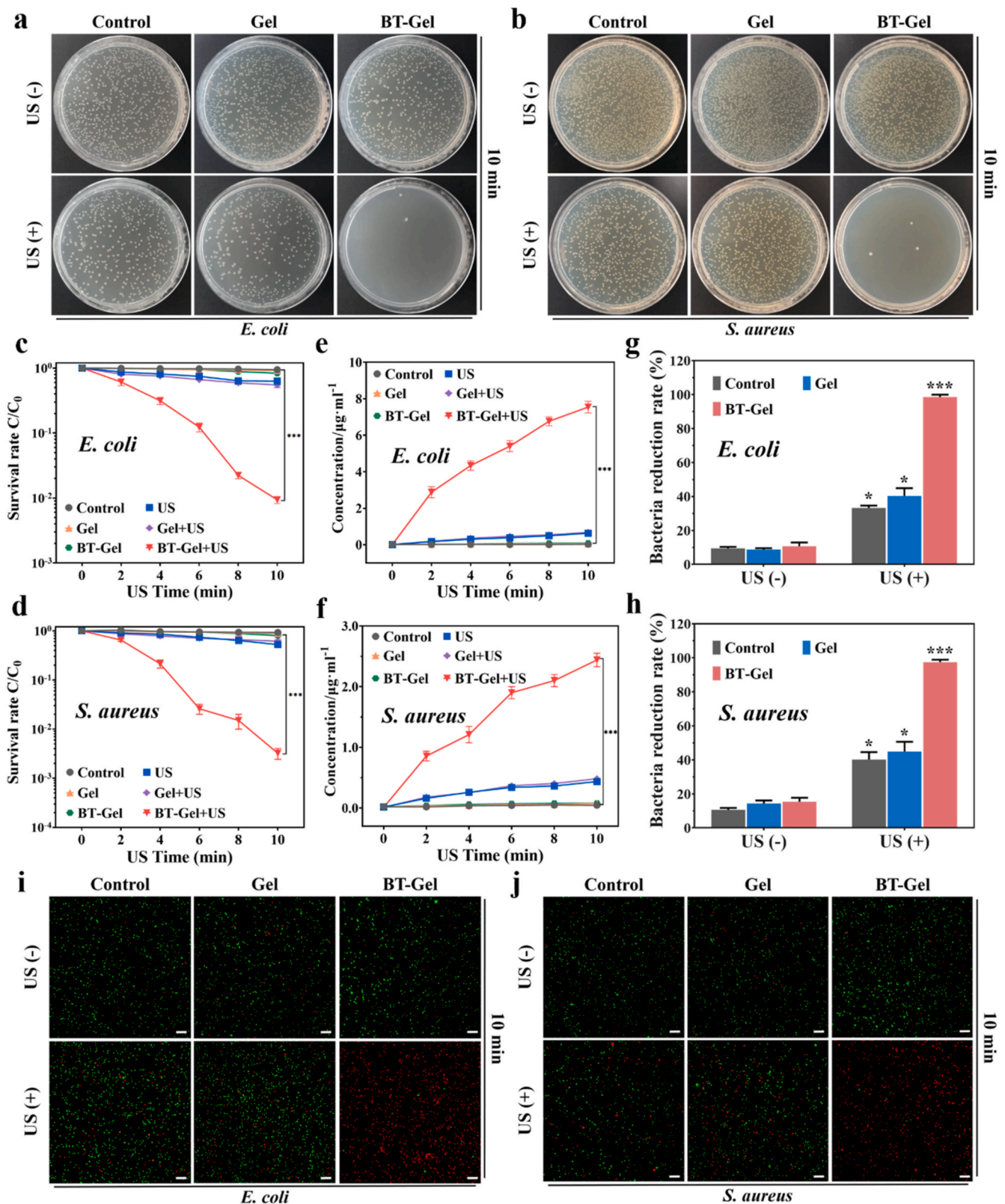
Fig. 4. *In vitro* **US-triggered piezocatalytic antibacterial therapy of BT-Gel against E. coli and S. aureus.** Representative photographs of (a) *E. coli* and (b) *S. aureus* CFUs grown on different samples with or without US irradiation. Quantitative analysis of bacterial survival rate of (c) *E. coli* and (d) *S. aureus* via agar plating method after different US treatment time. Quantitative analysis of protein leakage from (e) E. Coli and (f) *S. aureus*. Quantitative analysis of bacterial reduction rate of (g) *E. coli* and (h) *S. aureus* via live/dead staining in each group. Representative bacterial live/dead staining images of (i) *E. coli* and (j) *S. aureus*. Green fluorescence represented live bacteria stained with SYTO 9 and red represented dead bacteria stained with propidium iodide (PI). Scale bars: 100 μm *p < 0.05, **p < 0.01 and ***p < 0.001.

that in the group not exposed to US (Fig. 4g–4j). Particularly, when adhesive hydrogels containing the BT nanoparticles were exposed to US for 10 min, there were almost no viable bacteria present on the dressings. The proportion of bacteria with red fluorescence (dead bacteria) in the BT-Gel + US group reached as high as 98.5% and 97.4% for *E. coli* and *S. aureus*, respectively, exhibiting excellent antibacterial properties. It could be attributed to the massive sonodynamic generated ROS, which altered the permeability of bacteria membrane by inducing lipid peroxidation, and ultimately led to intracellular components leakage and the death of bacteria.

2.5. Multifunctional properties assay of the BT-Gel

2.5.1. Injectability and self-healing behavior

In situ crosslinked or injectable hydrogels exhibit promising applications as wound dressing materials, because they could automatically adapt to irregular wound shapes [45]. Static shear rate scans were performed using a rheometer to detect whether the hydrogels were shear-thinning. The viscosity of the hydrogels all decreased with the increase of shear rate (Fig. 5a), indicating the shear-thinning capacity of the hydrogels. Meanwhile, the hydrogel could be injected continuously through a syringe to draw the "NJU" letters and remained stable when the shear force was removed (inset of Fig. 5a). In addition, hydrogel dressings often encounter external mechanical forces after adhesion to the wound. Therefore, the hydrogels with self-healing ability will prolong their service time and improve the use security. To assess the self-healing behavior of these hydrogels, Gel$_{15}$ was selected as the model sample to conduct rheological recovery test and macroscopic self-healing test. The results of strain amplitude sweep test showed that the G′ and G″ of the hydrogel decrease sharply after a yield strain of about 300%, which was the intersection of G′ and G″ curve, indicating the critical point of hydrogel network collapse (Fig. 5b). The continuous step strain test was then performed to determine the self-healing behavior of the hydrogel. When a high dynamic strain (500%) beyond criticality was applied, the value of G′ experienced a sharp decrease to lower than that of G″. Once a lower strain (1%) was applied, the values of G′ and G″ could be recovered instantly almost to their original values even after four alternating cycles, demonstrating the autonomous healing behavior of the hydrogel (Fig. 5c). Based on the red pre-gelled disk-shaped hydrogel (stained with Rhodamine B), the macroscopic healing test of the Gel$_{15}$ hydrogel were performed. The cylindrical sample was cut in half and brought into contact without any external stimulation at ambient temperature. The cut hydrogel pieces healed rapidly on contact, and the healed sample showed no cracks and could be lifted by self-weight (Fig. 5d). The excellent autonomous healing capacity could be attributed to the Schiff base bond between the amino group in THM-APMH and the aldehyde in OHA, as well as high density H-bonds given by the unique tri-hydroxyl structure of THM-APMH (Fig. 5e).

2.5.2. Adhesive and hemostatic capacity

As a desirable skin wound dressing, in addition to the ingredients that could well promote the wound healing process, good adhesion performance is also essential [46]. The lap-shear test was performed to evaluate the adhesive properties of these hydrogels using porcine skins (Fig. 5f). As shown in Fig. 5g, all the hydrogels showed excellent bioadhesive performance, and the adhesive strength of the hydrogels increased from 49 to 79 kPa with the increase of THM-APMH content. It has been proved that the adhesion strength of hydrogel depends on the cohesion and interfacial adhesion of hydrogels. The trihydroxyl structure of THM increases the crosslinking density and improves the cohesion of hydrogels, and the increase of THM-APMH content enhances the interface adhesion of hydrogels, which should be a reasonable explanation for the maximum adhesion of Gel$_{15}$ hydrogel (Fig. 5h). For this reason, we selected Gel$_{15}$ as the representative to verify various biological properties of the adhesive hydrogels. Due to the frequent

movement of the human body, closed skin wounds may reopen. Therefore, we broke the hydrogel between the bonded porcine skins, then put the skin with the damaged hydrogel together again, and tested its adhesion 1 h after healing. The results showed that hydrogel had good autonomous healing property, while the adhesive strength of hydrogel after self-healing is not less than 80% of the initial adhesive strength (Fig. 5i), indicating that the hydrogel could adhere to the reopen wound and reseal the incision.

Hemostasis is the first stage of natural process of wound healing after injury. Hydrogels with excellent adhesion, serving as a sealant or physical barriers, could stick tightly to the wound site to accelerate bleeding-arrest, prevent bacterial invasion and exudation of body fluids [47–49]. A rat liver hemorrhaging model was applied to investigate the hemostatic performance of BT-Gel. As can be seen in Fig. 5j, there was a significant difference of blood loss between control and BT-Gel groups. The control group without any treatment had a blood loss of 952 mg, while the blood loss of the group treated with BT-Gel dramatically reduced to 100 mg, demonstrating the promising *in vivo* hemostasis capacity of BT-Gel. Meanwhile, the bleeding time in hemorrhaging liver mouse model was also measured. It turned out that the group treated with adhesive BT-Gel showed grossly reduced bleeding time compared with that of the control group. Furthermore, as illustrated in Fig. 5k and Fig. S5, the amount of bleeding in control group (with no treatment) obviously increased over time, while the bleeding at wound site in BT-Gel treatment group was completely controlled in a short time. In addition, there was no difference in hemostatic properties between Gel and BT-Gel *in vivo*, which proved that the BT nanoparticles will not weaken the hemostatic performance of Gel. The satisfactory hemostatic properties of BT-Gel in rat liver hemorrhaging model might be attributed to the strong adhesion between liver tissues and BT-Gel around the bleeding area, making it a promising candidate for anti-bleeding barrier in wound healing.

2.5.3. Biocompatibility and cell proliferation assay

Fibroblasts are a common cell type involved in the process of skin regeneration [50,51]. Therefore, mouse embryonic fibroblast (NIH-3T3) cells were employed to evaluate the effect of BT-Gel combined with US on the activity of fibroblast. The results of methyl thiazolyl tetrazolium (MTT) analysis at days 1, 3, and 7 showed that all groups displayed well cell viabilities (all more than 90%), revealing the satisfactory biocompatibility of these dressings (Fig. S6a). Similar results were obtained in live/dead staining test (Fig. 6a, S6b). It was worth noting that SDT had almost no effect on the cellular activity of NIH-3T3 cells. After 10 min US irradiation on the NIH-3T3 cells planted on BT-Gel, the survival rate of the cells was 98.7%, while that of BT-Gel without US group was 98.9%, demonstrating that the US-triggered piezocatalytic antibacterial therapy is safe for normal tissues and wound healing-related cells. To evaluate the effect of piezoelectric effect triggered by different US intensity on NIH-3T3 cell activity, live/dead staining was carried out in the same way after 2.0 and 2.5 W/cm^2 US stimulation (10 min, 1 MHz). As shown in Figure S6c~S6d, all groups of cells survived well, proving that the US intensity (1.5 W/cm^2) we adopted was within the biosafety range. The reason for the phenomenon that US-triggered piezocatalytic therapy has a side-effect on bacteria but not fibroblasts cells is probably that the respiratory chain of mammalian cells regulating electron transfer and ROS generation is in the intracellular organ's mitochondria [52]. Therefore, mammalian cells are more resistant to external ROS disturbance than bacteria [53]. More importantly, a controlled amount of ROS was generated by adjusting the US power to ensure both good biocompatibility and satisfactory bactericidal performance (Fig. S6).

2.6. Wound healing-related gene expression

Growth factors have a great impact on accelerating wound repair by regulating epithelial cell proliferation and migration. Epidermal growth factor (EGF), basic fibroblast growth factor (bFGF), and vascular
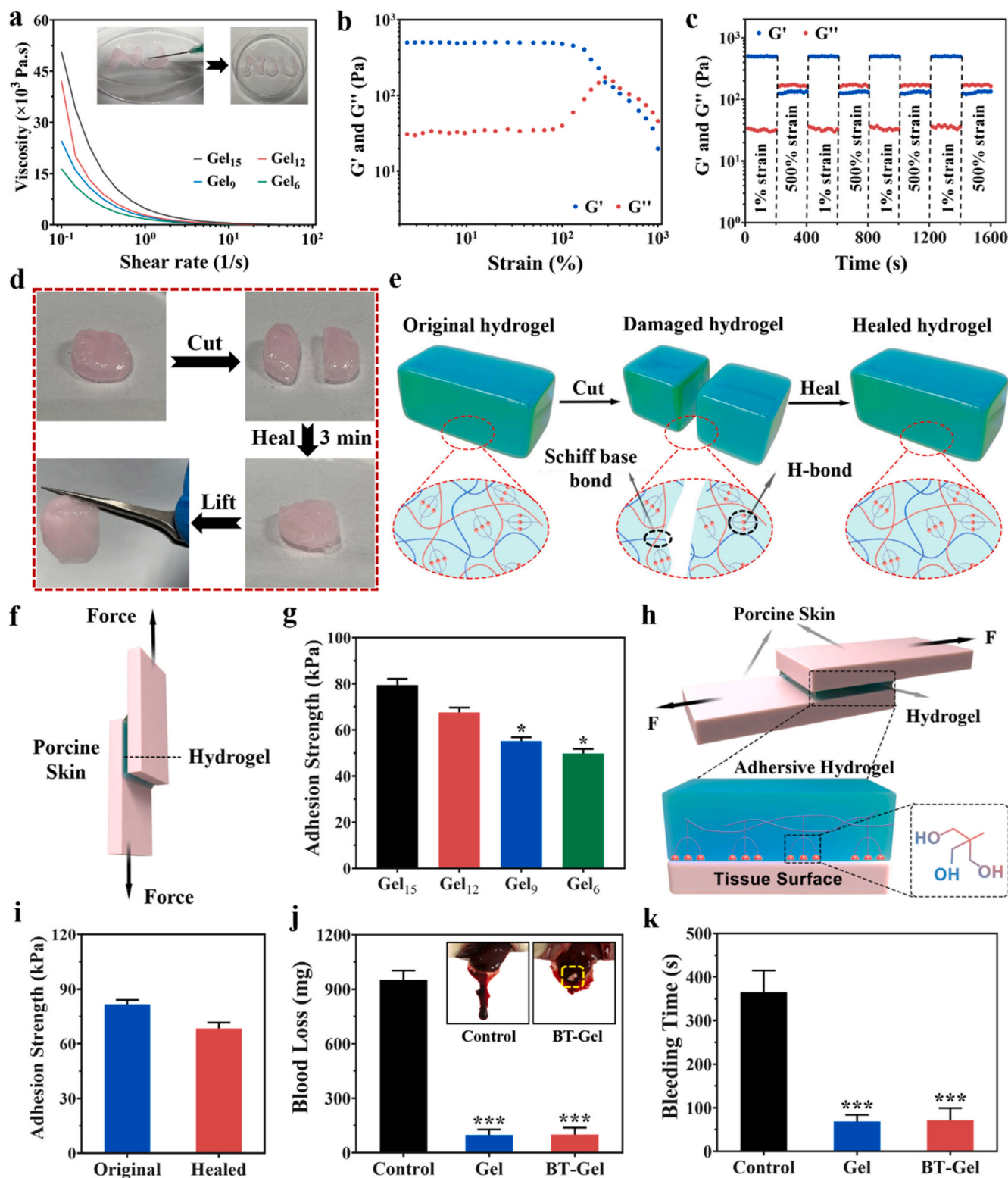
Fig. 5. Injectable, self-healing and adhesive properties of the hydrogels. (a) Shear-thinning test of the hydrogels (Inset: Display of injectability of the hydrogel through a syringe). (b) Strain amplitude sweep test of the multifunctional hydrogel with the strain ranging from 1% to 1000% (1 Hz). (c) Amplitude oscillation strain test of the hydrogel with alternated strain switching from 1% to 500% for four cycles. (d) Photographs of macroscopic autonomous healing ability of the hydrogel. (e) Schematic illustration of self-healing mechanism of the hydrogel. (f) Schematic diagram of the lap-shear test. (g) Adhesive strength of hydrogels with different THM-APMH concentration between porcine skins. (h) Schematic diagram of biological adhesion mechanism for the hydrogel. (i) Comparison of adhesive strength of the hydrogel before damage and 1 h after healing. (j) Blood loss of rat liver hemorrhage model (Inset: representative photographs of liver hemorrhage model treated with the bioadhersive hydrogel). (k) Bleeding time of rat liver hemorrhage model after different treatment.

endothelial growth factor (VEGF) are three main growth factors involved in the process of wound regeneration. In order to analyze the expression levels of tissue repairing-related genes, the NIH-3T3 cells were cultured with different interventions for 3 and 7 days (Fig. 6b). The results of quantitative reverse transcription polymerase chain reaction (qRT-PCR) showed that for Gel, Gel + US, and BT-Gel groups, the mRNA expressions of EGF, bFGF, and VEGF were higher than that of the control on the 3rd and 7th day (Fig. 6c–6e). The mRNA levels of the above genes were highest in the BT-Gel + US group. This phenomenon may be due to the local electrical stimulation on NIH-3T3 cells by surface potential generated by BT nanoparticles under US irradiation. It has been reported that the piezoelectric stimulation could enhance multiple growth factors expression, promote re-epithelialization and accelerate wound repair [54]. In addition, collagen is a key component of skin, and type I collagen (COL-I) and type III collagen (COL-III) are conducive to extracellular matrix reconstruction and wound regeneration [55]. Similar to the above three growth factor, remarkable increase of COL-I and COL-III expression was observed in the cells treated with BT-Gel + US as compared to other groups (Fig. 6f and g), revealing its enhanced recombination of collagen network at the genetic level. All the above results indicated that the BT-Gel combined with US irradiation could promote wound regeneration.
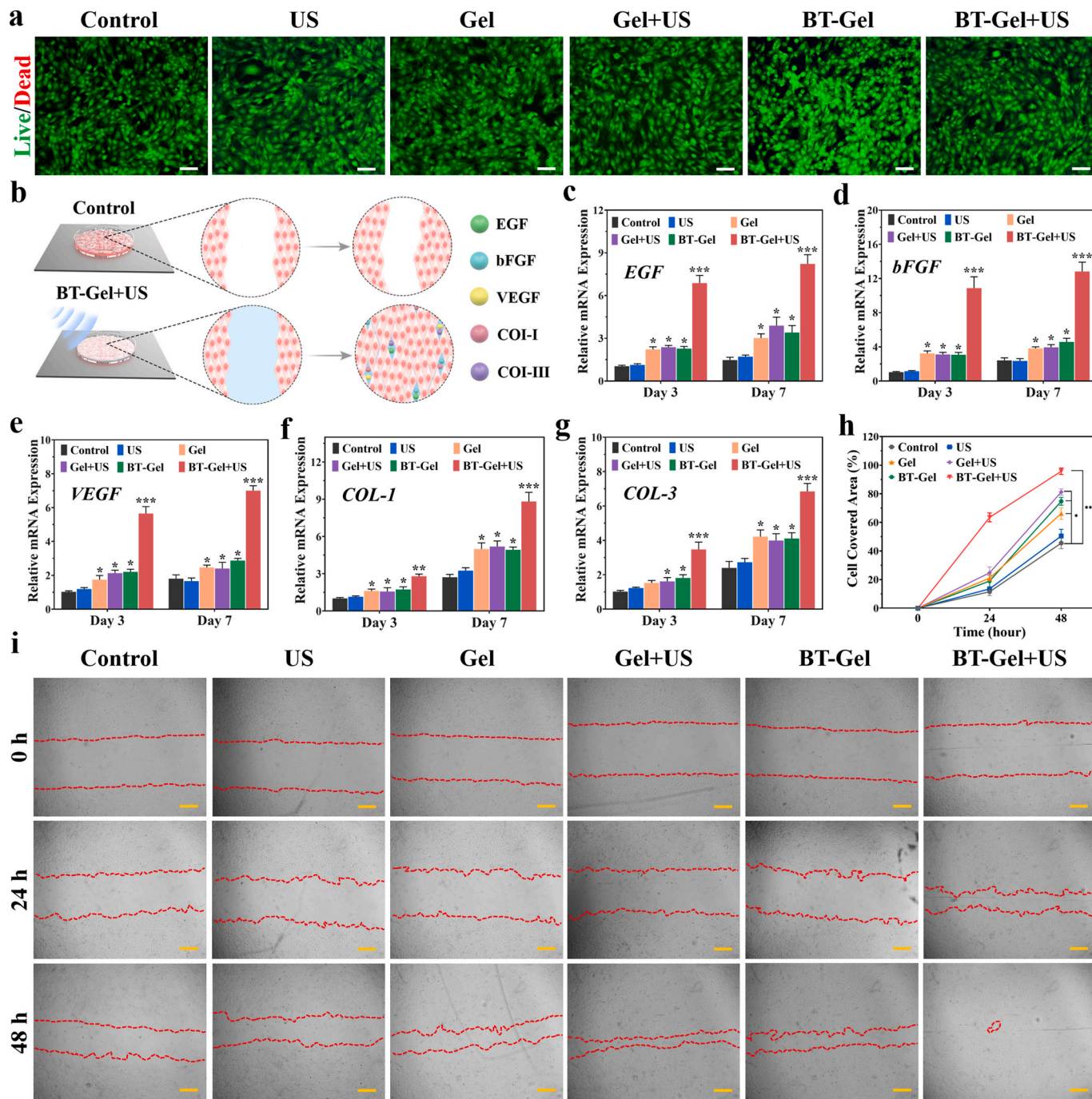

Fig. 6. Biocompatibility of the hydrogels and their role in promoting cytokine secretion and cell migration. (a) Representative live/dead staining images of NIH-3T3 cells after different treatments. Scale bars: 100 μm. (b) Schematic diagram of BT-Gel with US irradiation accelerating cell migration and stimulating tissue repairing-related gene expression. Quantitative analysis of mRNA expression of (c) EGF, (d) bFGF, (e) VEGF, (f) COL-I and (g) COL-III at day 3 and 7. (h) Quantitative analysis of cell migration. (i) Representative images of NIH-3T3 cell migration assay at different times. Scale bars: 200 μm *p < 0.05, **p < 0.01 and ***p < 0.001.

2.7. Cell migration assessment

Scratch assay was applied to assess the migration of NIH-3T3 cells cultured on the hydrogels. As illustrated in Fig. 6h and i, the cell migration rate of the BT-Gel + US group was significantly higher than that of other groups after 48 h of incubation, indicating that the process of piezoelectric antibacterial therapy triggered by US could not only kill bacteria, but also improve the migration of fibroblasts for wound repair. The reason for good cell distribution could be attributed to the suitable three-dimensional matrix-mimicking environment provided by the porous microstructures of bioadhesive hydrogels. Furthermore, it was reported that a proper concentration of ROS could adjust the local cytoskeleton at molecular level to promote cell migration by activating the redox signaling cascade [56]. Hence, ROS generated by BT-Gel under US irradiation *in vitro* could be considered as a synergistic factor for fibroblasts migration and wound closure.

2.8. In vivo infected wound healing

The wound healing efficiency of the BT-Gel with US stimulation was investigated *in vivo* by a full-thickness infected dermal wound. Twenty-four hours after the injection of *S. aureus* suspension in the defected site of rat with round skin wound (7 mm in diameter), the bacterial infection was confirmed by standard swab culture and solid agar plates counting (Fig. S7). Then, the BT-Gel was injected onto the incision as a sealant, followed by 10 min US irradiation for treatment (Fig. 7a). The wound repair results at different time were exhibited in Fig. 7b–7d, and the average wound closure rates at 9th day were 56.5%, 59.2%, 73.2%, 79.2%, 71.6%, and 98.8% for the control (treated with PBS), US, Gel, Gel + US, BT-Gel, and BT-Gel + US groups, respectively. The BT-Gel + US group showed the best wound repair among all the groups, indicated that US-triggered piezoelectric generated ROS had strong bacteria killing ability to improve wound healing *in vivo*. It was speculated that there should be other factors favoring cutaneous regeneration in addition to antibacterial effect. We observed that the mere US group showed a slightly better wound healing effect than the negative control group. The reason for this phenomenon may be the mechanical stimulation of skin with US, which could activate a fibronectin-dependent signaling pathway to promote fibroblast migration and reverse healing defects [57]. The Gel or BT-Gel treated incisions were also observed to have a faster closure speed during wound repair process, which could be attributed to the perfect shape-matching feature of the injectable hydrogels. Furthermore, the bioadhesive hydrogels had porous microstructures and good stickiness, providing a suitable matrix-mimicking environment for fibroblast proliferation and epidermal regeneration. In summary, the satisfactory wound repair efficiency of the BT-Gel with US irradiation was relative to comprehensive factors, including excellent bactericidal ability provided by ROS, bioadhesion, autonomous self-healing ability, and good biocompatibility favoring cell proliferation and migration. Moreover, except that the rats in the BT-Gel + US group grew steadily during the whole experiment, all the other rats suffered varying degrees of body weight loss at the initial of bacterial infection (Fig. S8). Further, H&E staining of the major organs was performed to assess the biocompatibility of the BT-Gel *in vivo*, and the results showed no significant change compared to the negative control group (Fig. S9).

To further analyze the epidermal regeneration and wound repair, H&E staining of granulation tissue over the wound bed was performed. In accordance with the results of wound closure rate, the wounds treated with the BT-Gel and US irradiation had narrower granulation tissue width and thicker regenerated epithelial tissues compared to others, indicating that the injectable hydrogel with desirable bactericidal capacity could improve the wound healing microenvironment (Fig. 7e, f, and 7h). Besides, the degree of skin regeneration in the groups treated with US and/or bioadhesive hydrogels was better than the control group, which also proved that both multifunction of the hydrogels

(injectability, adhesiveness and self-healing ability) and mechanical stimulation of US could accelerate wound recovery. In order to study the biological mechanism of incision repair process, Masson's trichrome staining was conducted to assess the collagen distribution at wound sites. As an integral part of skin, the synthesis, deposition, and orientation of collagen play a vital role in wound repair, and the presence of collagen deposition is beneficial to healing process [58,59]. Clearly, there were more deposited and highly oriented collagen structures in the BT-Gel + US group, displaying a better extracellular matrix remodeling and epithelial tissue reconstruction (Fig. 7g and i).

Inflammation was an important phase in wound healing and severe inflammatory reaction caused by bacteria infection would postpone the process of wound repair [60]. In the present study, typical pro-inflammation factors, including tumor necrosis factor α (TNF-α) and interleukin 6 (IL-6), were selected to assess the effectiveness of the BT-Gel with US in alleviating inflammation caused by infection. As depicted in immunohistochemical staining images (Fig. 8a-8d), fewer pro-inflammatory cytokines (brown color) were observed at the wound closure areas in the BT-Gel + US group compared with other groups, demonstrating the vital role of synergistic effect of the multifunctional hydrogel and US-triggered piezocatalytic therapy in protection against bacterial infection. On day 9th, granulation tissues in the wound sites were obtained to evaluate the protein expression of TNF-α and IL-6 by Western blot analysis. Consistent with the immunohistochemical staining results, the protein expressions of TNF-α and IL-6 were significantly down-regulated in the BT-Gel + US group (Fig. 8e-8g). Immunohistochemical staining of wound tissues for anti-inflammatory (interleukin-10, IL-10 and transforming growth factor-β, TGF-β) and pro-regenerative cytokines (VEGF) was also performed [61]. IL-10 and TGF-β were both significantly up-regulated in the BT-Gel + US group, indicating that the multifunctional hydrogel combined with low intensity US could alleviate the inflammation of infected wounds (Figs. S10a–10c). Furthermore, compared with other groups, the wounds in the BT-Gel + US group appeared more VEGF positive staining areas. These results demonstrated that wounds of rats in BT-Gel + US group have a faster closure speed during wound repair process (Figs. S10a and 10d).

Additionally, it was reported that angiogenesis was indispensable for tissue regeneration, allowing sufficient oxygen and nutrition supply along with favoring cytokine transport and cell migration [62–64]. Angiogenesis of the incision was determined by double immunofluorescent staining of platelet endothelial cell adhesion molecule-1 (CD-31, marker of vascular endothelial cell) and α smooth muscle actin (α-SMA, marker of vascular smooth muscle cell) [65,66]. The co-location spatial relationship between CD-31 and α-SMA staining signified the mature neovascularization and the density of blood vessel in wound bed was then estimated. In consistency with the results of epithelial regeneration, the wounds in the injectable hydrogels and/or US treatment groups appeared more positive staining of CD-31 and α-SMA than in the PBS group, especially the most in the BT-Gel + US group, illustrating its great acceleration of growth of new capillaries into the wound (Fig. 8h and i). The better angiogenesis of wounds in the BT-Gel + US group may be mainly due to a synergistic effect between multifunctional features of the hydrogels and antibacterial activity offered by sonodynamic generated ROS.

3. Conclusion

In summary, we have developed a piezoelectric nanoparticles-wrapped multifunctional hydrogel for wound healing in the assistance with sonodynamic antimicrobial therapy. The dynamic Schiff base interaction and high density of H-bonds endowed the hydrogel with rapid gelation, stable rheological property, good injectability, bioadhesiveness, and self-healing capacity, providing a suitable three-dimensional matrix-mimicking microenvironment conducive to cell migration and epithelial regeneration. For *In vitro* experiments, it was
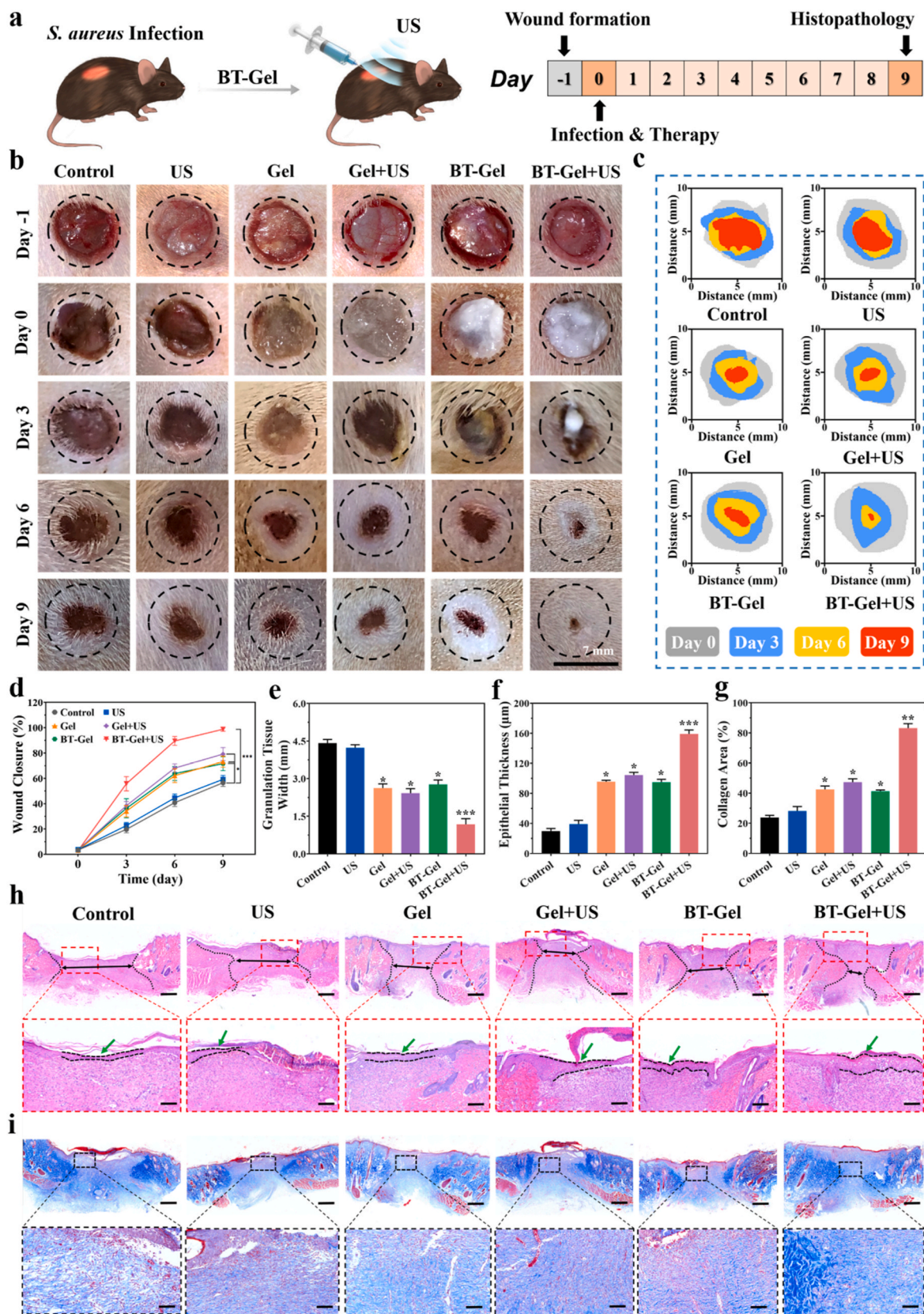
Fig. 7. In vivo S. aureus-infected wound closure assessment. (a) Schematic diagram of BT-Gel with US irradiation in the treatment of infectious wounds in rats. (b) Representative photographs of infected wounds at different times during the treatment. Scale bars: 7 mm. (c) Schematic images of wound closure trace during 9 days. (d) Relative wound closure area of the rats from day 0 to day 9 after different interventions. Quantitative analysis of (e) granulation tissue width and (f) epithelial thickness on day 9. (g) Quantitative analysis of collagen deposition estimated from images of Masson trichrome staining. (h) Representative H&E staining of the wound beds on day 9. Scale bars: 300 μm. (i) Representative Masson trichrome staining photographs of the wound sites in each group. Scale bars: 300 μm *p < 0.05, **p < 0.01 and ***p < 0.001.
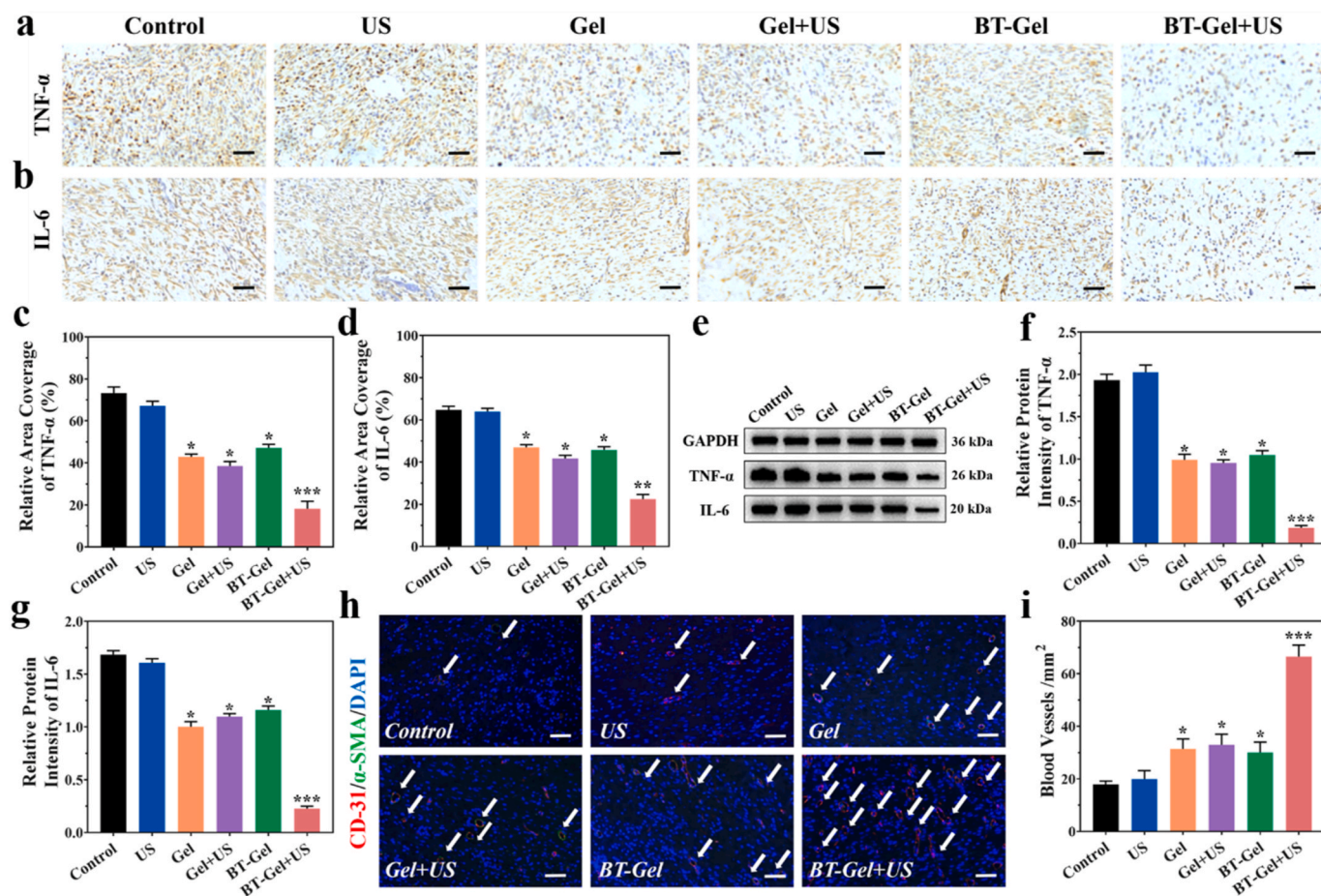
Fig. 8. Inflammation and angiogenesis evaluation at wound sites. (a) Representative images of immunostaining for TNF-α and (b) IL-6. Scale bars: 100 μm. (c) Quantitative data of the relative area coverage of TNF-α and (d) IL-6. (e) Western blot analysis of TNF-α and IL-6 protein expression. (f) Statistical analysis of relative protein intensity of TNF-α and (g) IL-6. (h) Representative images of double-label immunofluorescence staining of CD-31 and α-SMA. The white arrows indicate blood vessels. (i) Quantitative analysis of the blood vessel density. Scale bars: 20 μm *p < 0.05, **p < 0.01 and ***p < 0.001.

noted that the BT-Gel under US irradiation exhibited excellent antibacterial activity by rapidly piezoelectric generated ROS. Moreover, its remarkable curative effect on wound repair was demonstrated by an infected derma defect model in terms of wound closure rate, granulation tissue regeneration, collagen disposition, inflammation alleviation, and angiogenesis. With all the promising properties mentioned above, the US-assisted antibacterial hydrogel could effectively accelerate the healing of infected cutaneous incisions, creating a novel designing concept for wound dressing material by combining multifunctional hydrogels and US-triggered piezocatalytic therapy to synergistically promote the wound closure. More importantly, this composite hydrogel exhibits great application potential in the treatment of deep infection that cannot be covered by traditional methods, rather than being limited to the treatment of superficial infected wounds.

4. Experimental section

4.1. Preparation of the BT nanoparticles

Firstly, $Ba(OH)_2 \cdot H_2O$ (12.85 g, Sigma-Aldrich) was weighed and dissolved in 25 mL of deionized water to obtain solution A. Then tetrabutyl titanate (17.02 g, Sigma-Aldrich) was weighed and dissolved in 20 mL of ethanol, and 7 mL of 35% ammonia solution was added to obtain solution B. After mixing A and B solutions, 5 mL triethanolamine (Aladdin) was mixed and added into 100 mL Teflon reactor. After 48 h of reaction at 200 °C, the resulting powder was washed and dried to get white powder. Finally, the BT nanoparticles were transformed from

cubic phase to tetragonal phase with piezoelectric catalytic effect by thermal annealing. During thermal treatment, the BT powder obtained was heated in a tubular furnace at 800 °C for 10 h and then grinded into fine powder after natural cooling.

4.2. Preparation of the BT-Gel

THM-APMH was synthesized by free radical polymerization method. THM and APMH were dissolved in deionized water under nitrogen atmosphere, and then ammonium persulfate (APS, Aladdin) was added to initiate polymerization at 60 °C. After 1 h, the reaction temperature was raised to 70 °C for 24 h. THM-APMH was obtained followed by dialysis and freeze-drying. OHA was synthesized by the oxidation of *cis*-diol in HA (Sigma-Aldrich) by $NaIO_4$ (Aladdin) and then purified by freezing method. OHA/THM-APMH hydrogels were fabricated by mixing OHA and THM-APMH, and several hydrogels were prepared with different contents of THM-APMH. The BT nanoparticles were dispersed to THM-APMA and OHA solution (1 mg/mL) and mixed with a double-headed syringe to form the hydrogels for later use.

4.3. Characterization of the BT nanoparticles

Scanning electron microscope (SEM) images were acquired on a field-emission Magellan 400 microscope. The hydrodynamic diameter of the prepared BT nanoparticles was measured by dynamic light scattering (DLS) technique (DelsaMax PRO, Beckman Coulter). X-ray diffraction (XRD) patterns were measured by a Philips X'Pert diffractometer with

Cu Kα radiation generated at 40 kV and 40 mA. The piezoelectricity of the BT nanoparticles was measured using the atomic force microscope (AFM, dimension icon, Bruker).

4.4. Characterization of the BT-Gel

Chemical structures of the reaction products were examined by a Nicolet 6700 fourier-transform infrared (FTIR) spectrometer (Thermo Scientific) and a Bruker Ascend 400 MHz nuclear magnetic resonance (NMR) instrument.

4.5. Swelling ratio test

The *in vitro* swelling test was used to assess the swelling ratio and stability of the OHA/THM-APMH hydrogels. Firstly, the hydrogel samples were freeze-dried and the dry weight of the sample was recorded (W_0). Then, to simulate physiological conditions, the hydrogels were placed in a sealed tube containing 5 mL of PBS (pH = 7.4) at 37 °C. When reaching the pre-determined time interval, the samples were taken out of PBS, and the surface moisture was removed with filter paper before the hydrogels were weighed (W_t). The swelling ratio was calculated based on the following equation:

$$\text{Swelling ratio (\%)} = (W_t - W_0) / W_0 \times 100$$

4.6. In vitro ROS detection

Rhodamine B was selected to test ROS generation capacity. Firstly, 5 mg of the BT nanoparticles were dispersed in 5 mL of Rhodamine B aqueous solution (10 mg L^{-1}). The resulting mixed solution was then stirred for 60 min to achieve an adsorption-desorption equilibrium between the BT nanoparticles and Rhodamine B. In order to study the piezoelectric catalytic effect of the BT nanoparticles under different US irradiation time (0, 2, 4, 6, 8, 10 min, 1.5 W/cm^2, 1 MHz), the suspension samples were collected regularly and centrifuged to obtain transparent solution. To assess the piezocatalytic performance of the BT-Gel, 5 mL of the hydrogel (1% w/v BT) was uniformly coated on a 21 cm^2 Petri dish, and 5 mL of Rhodamine B (10 mg L^{-1}) was then added. The remaining surface solution was collected after the corresponding time of US irradiation. Finally, the residual Rhodamine B concentration in the clean solution was determined by ultraviolet–visible spectrophotometer. Untreated deionized water was used as the control.

The reactive oxygen species produced by US-triggered piezoelectric catalyst were detected by electron spin resonance (ESR) technique using a Bruker E500 ESR spectrometer. 5, 5-dimethyl-1-pyrroline N-oxide (DMPO) was adopted as the spin-trapping agents of •OH and •O$_2^-$, respectively. The following four groups of samples were tested by the ESR spectrometer at ambient temperature including the control (DMPO, 1 mg mL^{-1}), US (DMPO + US), BT (DMPO + BT), and BT + US (DMPO + BT + US) groups.

4.7. Antibacterial test in vitro

Gram-negative *E. coli* (ATCC 25922) and Gram-positive *S. aureus* (ATCC 22004) kindly gifted from Dr. Canwen Chen (Affiliated Jinling Hospital, Medical School of Nanjing University) were used to test the antibacterial ability of the BT-Gel as previously described. In brief, 15 μL of prepared bacterial suspensions (10^6/mL) were added onto 500 μL of the BT-Gel surface in a 24-well cell plate. After different time of US irradiation (1.5 W/cm^2, 1 MHz) from 0 to 2, 4, 6, 8, and 10 min, the 24-well plate was put into an incubator at 37 °C for 2 h. Next, the bacteria suspensions were separated from the surface by 1 mL of the sterilized PBS and diluted to an appropriate concentration (~100 times) before the spread plate operation. Subsequently, bacterial survival rate was

measured by counting the number of bacterial colony forming units (CFUs) in the solid agar plates after 18 h of culture. Tests were repeated three times for each group, and survival rate of bacteria were calculated by the following equation:

$$\text{Bacteria survival rate (\%)} = (C/C_0) \times 100$$

where C was the bacteria colonies number of experiment groups, and C_0 was the number of the control group.

After filtration of the above bacterial suspensions with 0.22 μm filters, the concentration of bacterial protein leakage after treatment with different US times was detected using a Pierce micro BCA protein detection kit (23235, Thermo Fisher Scientific). Additionally, in order to assess the survival of bacteria after the above treatment, each sample was stained with LIVE/DEAD *Bac*Light Bacterial Viability Kit (L7012, Thermo Fisher Scientific) according to the protocol from manufacturer, and observed on a high-resolution microscope (Thunder Imaging Systems, Leica), in which the dead bacteria were stained in red fluorescence by PI while the living bacteria in green fluorescence by SYTO 9.

$$\text{Bacteria reduction rate (\%)} = (N/N_0) \times 100,$$

where N was the number of the dead bacteria, and N_0 was the total number of the dead and living bacteria.

4.8. Rheological Data and injectability

The rheological characteristics of the hydrogel were measured by TA rheometer (DHR-2). During rheological experiment, a solution of 500 μL of hydrogel precursor mixture was placed between parallel plates with diameters of 20 mm and spacing of 1 mm. The stiffness of the hydrogels with different THM-APMH and OHA ratios was studied by the time sweep test at a constant frequency of 1 Hz, and the deformation was 1%. Shear-thinning test was carried out with Gel$_{15}$. The shear rate was in the range of 0.1–100 1/s, the frequency was maintained at 1 Hz, and the strain was maintained at 1%.

4.9. Self-healing behavior

The self-healing ability of the adhesive hydrogel was evaluated by rheological recovery test and macro self-healing test. First, strain amplitude sweep test was performed in the strain range of 0.1%–1000% to determine the maximum critical strain that the hydrogel could withstand. Then, an original hydrogel was used to test the self-healing behavior by alternating strain scanning at a fixed angular frequency (1 rad s). The amplitude oscillation strain was converted from small strain (1%) to large strain (500%) with 400 s time interval of each strain test, and 4 cycles were carried out. The disc-shaped hydrogel was dyed with Rhodamine B and cut into two pieces. Two pieces of hydrogel were then put together without external stimulation. Self-healing was confirmed by the capacity of the healed disc-shaped hydrogel to hold its original structure when suspended under gravity.

4.10. Adhesive ability

The adhesion strength was evaluated by a lap-shear test. In brief, fresh porcine skin was cut into 1 cm × 3 cm rectangles and immersed in PBS for later use. The hydrogel precursor solutions were coated on the surface of a fresh porcine skin, and another porcine skin of the same size was then attached to the solution (The adhesion area was 1cm × 1 cm). Finally, adhesion strength was measured by a universal mechanical testing machine (CMT4202) equipped with a 100 N load cell at a speed of 2 mm/min.

4.11. In vivo hemostatic ability test

A rat liver hemorrhaging model (Sprague Dawley rats, 200–220 g,

female) was used to evaluate the hemostatic effect of the Gel and BT-Gel. Briefly, the liver of SD rat was exposed through abdominal incision after anesthetized with isoflurane. After carefully removing the surrounding tissue fluid, the liver was placed on a pre-weighed filter paper. A 5 mm incision was cut by micro scissors to induce liver bleeding and then 500 μL of the BT-Gel was immediately injected to cover the bleeding site as a hemostatic agent. After complete hemostasis, the increased weight of filter paper and bleeding time were recorded and compared with the control group (without any treatment after liver hemorrhaging). The liver bleeding site was photographed at 0, 5, 15, 30, and 60 s after bleeding, respectively.

4.12. Cell Culture and viability

To assess the cytotoxicity of the hydrogel dressings *in vitro*, NIH-3T3 cells (CL-0171, Procell Life Science & Technology) were seeded onto the Gel and BT-Gel with specific mediums provided by the manufacturer after corresponding intervention. For the groups with US irradiation, the duration was 10 min (1.5 W/cm^2, 1 MHz). After 1, 3, and 7 days of co-culture, methyl thiazolyl tetrazolium (MTT) cell growth assay kit (CT02, Sigma) was used for cell proliferation assessment according to the product specification. Next, NIH-3T3 cells of the six groups (control, US, Gel, Gel + US, BT-Gel, and BT-Gel + US) were stained with live/dead cell double staining kit (Calcein-AM/Propidium Iodide, Sigma) to detect the cell viability at day 3, and all fluorescent photographs were observed by a microscope (Thunder Imaging Systems, Leica).

4.13. Wound healing-related gene expression

The expression level of healing-related genes (EGF, bFGF, VEGF, COL-I, and COL-III) was analyzed by quantitative real-time polymerase chain reaction (qRT-PCR). Total RNA was extracted from the NIH-3T3 cells using Trizol reagent (Invitrogen), and then quantified with the NanoDrop 2000 spectrophotometer (Thermo Scientific). The RNA samples were reversely transcribed to cDNA using the PrimeScript RT Master Mix (TaKaRa). qRT-PCR was performed on a BIO-RAD q-PCR system with SYBR Green Master Mix (TaKaRa) based on the protocol provided by the manufacturer. The results were analyzed by the comparative cycle-threshold method, and the primer sequences are listed in Table S1.

4.14. Scratch assay

The effect of US exposure and the hydrogels on cell migration was investigated by scratch assay according to standard protocols. Briefly, NIH-3T3 cells were implanted into a 6-well plate with a concentration of about 10^6/well and placed in an incubator for 24 h. After cell planking, a scratch was made with a sterilized micro pipette tip. In order to make the remaining gap clearly visible, PBS was used to rinsed the plates for 3 times to remove the falling cells. Then, the previous culture medium was replaced by serum-free high-glucose DMEM after corresponding intervention (10 min US irradiation for the groups with US, 1.5 W/cm^2, 1 MHz). Experimental images were observed and captured with a microscope (Thunder Imaging Systems, Leica) after 0, 24, and 48 h of incubation, respectively. The migration rate was calculated by comparing the cell coverage at corresponding time points in scratch with the assistance of Image J Software.

4.15. In vivo Antibacterial and wound healing

A full-thickness S. aureus-infected wound rat model (Sprague Dawley rats, 200–220 g, female) was employed to evaluate the effect of the BT-Gel with US on infected wound healing as previously reported. Briefly, a round full-thickness cutaneous wound with a diameter of 7 mm was made on the back of each SD rat using a skin ring drill after anesthesia and shaving. Then, 15 μL of *S. aureus* suspensions (10^6 CFU/

mL) was injected to the defected area to cause infection. After 24 h (recorded as day 0), the wound infection was confirmed by routine swab culture and subsequent spread solid agar plates operation. The bacterial CFU on the plate were recorded and analyzed. Next, the successfully infected rats were randomly divided into six groups: negative control (PBS), Gel, BT-Gel, US, Gel + US, and BT-Gel + US groups. Different interventions were carried out on each wound and US irradiation duration was 10 min (1.5 W/cm^2, 1 MHz). In order to monitor the infected-wound healing process, the wound area was photographed on days 0, 3, 6, and 9. The wound closure was calculated by the following equation with Image J software: The wound closure (%) = (wound area on day 0 - wound area on certain day)/(wound area on day 0) × 100.

4.16. Histological analysis

To assess wound closure and epidermal regeneration, skin tissues were harvested at 9 days after treatment and sliced for histological analysis. Specifically, the tissue samples were taken out and fixed with 4% paraformaldehyde for 1 h and then embedded in paraffin after dehydration. Serial sections with a thickness of 5 μm were obtained by microtome for H&E staining, Masson trichrome staining, and immuno-fluorescence staining. The immunohistochemistry of TNF-α and IL-6 were conducted to assess wound inflammation, and CD-31/α-SMA double labeled immunofluorescence staining was performed to evaluate wound blood vessels regeneration. Additionally, to estimate the biocompatibility of the adhesive hydrogels *in vivo*, the major organs, including heart, liver, spleen, lung, and kidney, of SD rats were also obtained and sectioned for H&E staining. All images obtained from the above sections were recorded by a fluorescence microscope (Thunder Imaging Systems, Leica).

4.17. Western blot analysis

Western blot assay was used to detect the expression of inflammation related proteins (TNF-α and IL-6) in wound tissues of rats in each group. The proteins were extracted using RIPA Lysis Buffer (Beyotime Biotechnology) and separated by 10% SDS-PAGE (Epizyme Biomedical). Western blot was performed according to the primary antibody for TNF-α (1:1000, ab215188, Abcam) and IL-6 (1:1000, ab233706, Abcam). Peroxidase-conjugated goat anti-rabbit IgG (1:4000, Proteintech) was used as the secondary antibody.

4.18. Statistical analysis

All data were analyzed with standardized statistical software (SPSS, version 20.0, Chicago, IL, USA). Experimental results were shown with mean ± SD. Student's t-test and One-way ANOVA were performed for comparison analysis. Significance levels were set at $* \ p < 0.05$, $**p < 0.01$, and $***p < 0.001$.

Data and materials availability

All data needed to evaluate the conclusions in the paper are present in the paper and/or the Supplementary Materials. Additional data related to this paper may be requested from the authors.

Ethics approval and consent to participate

Animals were treated in accordance with the Guide for Care and Use of Laboratory Animals, approved by **the Animal Ethics Committee of Affiliated Drum Tower Hospital, Medical School of Nanjing University (Approval No.:YXZXA2016009).** All the animal operations complied with the institutional and Chinese government guidelines for the care and use of experimental animals.

CRediT authorship contribution statement

Dun Liu: Conceptualization, Methodology, Resources, Validation, Formal analysis, Writing – original draft. **Lei Li:** Conceptualization, Methodology, Software, Writing – original draft. **Ben-Long Shi:** Methodology, Data curation, Visualization. **Bo Shi:** Resources, Data curation. **Ming-Ding Li:** Resources. **Yong Qiu:** Supervision, Funding acquisition. **Di Zhao:** Conceptualization, Project administration. **Qun-Dong Shen:** Writing – review & editing, Supervision, Funding acquisition. **Ze-Zhang Zhu:** Writing – review & editing, Supervision, Project administration, Funding acquisition.

Declaration of competing interest

The authors declare no conflict of interest.

Acknowledgements

None.

Supporting Information

Supporting Information is available from the author.

Appendix A. Supplementary data

Supplementary data to this article can be found online at https://doi.org/10.1016/j.bioactmat.2022.11.023.

References

[1] A.J. Singer, R.A. Clark, Cutaneous wound healing, N. Engl. J. Med. 341 (10) (1999) 738–746.

[2] B. Yu, S.Y. Kang, A. Akthakul, et al., An elastic second skin, Nat. Mater. 15 (8) (2016) 911–918.

[3] Y.S. Zhang, A. Khademhosseini, Advances in engineering hydrogels, Science 356 (6337) (2017).

[4] L. Shi, X. Liu, W. Wang, L. Jiang, S. Wang, A self-pumping dressing for draining excessive biofluid around wounds, Adv Mater 31 (5) (2019), e1804187.

[5] X. Mao, R. Cheng, H. Zhang, et al., Self-healing and injectable hydrogel for matching skin flap regeneration, Adv. Sci. 6 (3) (2019), 1801555.

[6] X. Zhao, H. Wu, B. Guo, R. Dong, Y. Qiu, P.X. Ma, Antibacterial anti-oxidant electroactive injectable hydrogel as self-healing wound dressing with hemostasis and adhesiveness for cutaneous wound healing, Biomaterials 122 (2017) 34–47.

[7] Y. Bu, L. Zhang, J. Liu, et al., Synthesis and properties of hemostatic and bacteria-responsive in situ hydrogels for emergency treatment in critical situations, ACS Appl. Mater. Interfaces 8 (20) (2016) 12674–12683.

[8] C. Dhand, M. Venkatesh, V.A. Barathi, et al., Bio-inspired crosslinking and matrix-drug interactions for advanced wound dressings with long-term antimicrobial activity, Biomaterials 138 (2017) 153–168.

[9] Feng J, Yao F, Liu X, Tian S, Lan S, Xiong Y. Significant Improvement and Mechanism of Ultrasonic Inactivation to Escherichia coli with Piezoelectric Effect of Hydrothermally Synthesized T-BaTiO3.

[10] P. Zhu, Y. Chen, J. Shi, Piezocatalytic tumor therapy by ultrasound-triggered and BaTiO(3) -mediated piezoelectricity, Adv Mater 32 (29) (2020), e2001976.

[11] D. Sun, X. Pang, Y. Cheng, et al., Ultrasound-switchable nanozyme augments sonodynamic therapy against multidrug-resistant bacterial infection, ACS Nano 14 (2) (2020) 2063–2076.

[12] R. Wang, Q. Liu, A. Gao, et al., Recent developments of sonodynamic therapy in antibacterial application, Nanoscale 14 (36) (2022) 12999–13017.

[13] J. Chen, H. Luo, Y. Liu, et al., Oxygen-self-produced nanoplatform for relieving hypoxia and breaking resistance to sonodynamic treatment of pancreatic cancer, ACS Nano 11 (12) (2017) 12849–12862.

[14] F. Chen, H. Huang, L. Guo, Y. Zhang, T. Ma, The role of polarization in photocatalysis, Angew Chem. Int. Ed. Engl. 58 (30) (2019) 10061–10073.

[15] C. Pan, J. Zhai, Z.L. Wang, Piezotronics and piezo-phototronics of third generation semiconductor nanowires, Chem Rev 119 (15) (2019) 9303–9359.

[16] Z. Li, X. Yuewei, X. Yumeng, et al., Injectable self-healing antibacterial bioactive polypeptide- based hybrid nanosystems for efficiently treating multidrug resistant infection, skin-tumor therapy, and enhancing wound healing, Adv. Funct. Mater. 29 (22) (2019), 1806883.1-.180688311.

[17] M. Wang, C. Wang, M. Chen, et al., Efficient angiogenesis-based diabetic wound healing/skin reconstruction through bioactive antibacterial adhesive ultraviolet shielding nanodressing with exosome release, ACS Nano 13 (9) (2019) 10279–10293.

[18] D. Gan, T. Xu, W. Xing, et al., Mussel-inspired contact-active antibacterial hydrogel with high cell affinity, toughness, and recoverability, Adv. Funct. Mater. 29 (1) (2019), 1805964.1-.180596411.

[19] L. Li, B. Yan, J. Yang, L. Chen, H. Zeng, Novel mussel-inspired injectable self-healing hydrogel with anti-biofouling property, Adv Mater 27 (7) (2015) 1294–1299.

[20] Y. Wang, G. Chen, H. Zhang, C. Zhao, L. Sun, Y. Zhao, Emerging functional biomaterials as medical patches, ACS Nano 15 (4) (2021) 5977–6007.

[21] M.M. Hasani-Sadrabadi, P. Sarrion, S. Pouraghaei, Y. Chau, A. Moshaverinia, An engineered cell-laden adhesive hydrogel promotes craniofacial bone tissue regeneration in rats, Sci. Transl. Med. 12 (534) (2020), eaay6853.

[22] Y. Wang, L. Shang, G. Chen, L. Sun, X. Zhang, Y. Zhao, Bioinspired structural color patch with anisotropic surface adhesion, Sci. Adv. 6 (4) (2020), eaax8258.

[23] Q. Shi, X. Luo, Z. Huang, et al., Cobalt-mediated multi-functional dressings promote bacteria-infected wound healing, Acta Biomater. 86 (2019) 465–479.

[24] M.C. Giano, Z. Ibrahim, S.H. Medina, et al., Injectable bioadhesive hydrogels with innate antibacterial properties, Nat. Commun. 5 (2014) 4095.

[25] Jh A, Ms A, Yl A, Bga B. Conductive adhesive self-healing nanocomposite hydrogel wound dressing for photothermal therapy of infected full-thickness skin wounds - ScienceDirect. Chem. Eng. J.. 394.

[26] G.P. Maier, M.V. Rapp, J.H. Waite, J.N. Israelachvili, A. Butler, BIOLOGICAL ADHESIVES. Adaptive synergy between catechol and lysine promotes wet adhesion by surface salt displacement, Science 349 (6248) (2015) 628–632.

[27] M.F.P. Graça, S.P. Miguel, C.S.D. Cabral, I.J. Correia, Hyaluronic acid-Based wound dressings: a review, Carbohydr. Polym. 241 (2020), 116364.

[28] Seonki, Hong, Kisuk, et al., Hyaluronic acid catechol: a biopolymer exhibiting a pH-dependent adhesive or cohesive property for human neural stem cell engineering, Adv. Funct. Mater. 23 (14) (2013) 1774–1780.

[29] K. Ren, Y. Cheng, C. Huang, R. Chen, Z. Wang, J. Wei, Self-healing conductive hydrogels based on alginate, gelatin and polypyrrole serve as a repairable circuit and a mechanical sensor, J. Mater. Chem. B 7 (37) (2019) 5704–5712.

[30] J. Qu, X. Zhao, Y. Liang, T. Zhang, P.X. Ma, B. Guo, Antibacterial adhesive injectable hydrogels with rapid self-healing, extensibility and compressibility as wound dressing for joints skin wound healing, Biomaterials 183 (2018) 185–199.

[31] B. Yang, J. Song, Y. Jiang, et al., Injectable adhesive self-healing multicross-linked double-network hydrogel facilitates full-thickness skin wound healing, ACS Appl. Mater. Interfaces 12 (52) (2020) 57782–57797.

[32] D. Zhao, P. Feng, J. Liu, et al., Electromagnetized-nanoparticle-modulated neural plasticity and recovery of degenerative dopaminergic neurons in the mid-brain, Adv. Mater. 32 (43) (2020).

[33] P. Zhu, Y. Chen, J. Shi, Piezocatalytic tumor therapy by ultrasound-triggered and BaTiO3-mediated piezoelectricity, Adv. Mater. 32 (29) (2020).

[34] X. Dong, L. Lin, J. Chen, et al., A serum-tolerant hydroxyl-modified polyethylenimine as versatile carriers of pDNA/siRNA, Macromol. Biosci. 13 (4) (2013) 512–522.

[35] J. Chen, D. Wang, L.H. Wang, et al., An adhesive hydrogel with "Load-Sharing" effect as tissue bandages for drug and cell delivery, Adv Mater 32 (43) (2020), e2001628.

[36] S. Katzir, The discovery of the piezoelectric effect, Arch. Hist. Exact Sci. 57 (1) (2003) 61–91.

[37] J. Wu, Q. Xu, E. Lin, et al., Insights into the role of ferroelectric polarization in piezocatalysis of nanocrystalline BaTiO(3), ACS Appl. Mater. Interfaces 10 (21) (2018) 17842–17849.

[38] D. Zhao, P.J. Feng, J.H. Liu, et al., Electromagnetized-nanoparticle-modulated neural plasticity and recovery of degenerative dopaminergic neurons in the mid-brain, Adv Mater 32 (43) (2020), e2003800.

[39] C. Liu, D. Kong, P.C. Hsu, et al., Rapid water disinfection using vertically aligned MoS2 nanofilms and visible light, Nat. Nanotechnol. 11 (12) (2016) 1098–1104.

[40] Giuntini, Francesca, Loredana Serpe, Sonodynamic antimicrobial chemotherapy: first steps towards a sound approach for microbe inactivation, J. Photochem. Photobiol. B Biol.: Official Journal of the European Society for Photobiology 150 (2015) 44–49.

[41] Z. Zhou, J. Song, L. Nie, X. Chen, Reactive oxygen species generating systems meeting challenges of photodynamic cancer therapy, Chem. Soc. Rev. 45 (2016).

[42] M. Wu, Y. Ding, L. Li, Recent progress in the augmentation of reactive species with nanoplatforms for cancer therapy, Nanoscale 11 (42) (2019) 19658–19683.

[43] M.A. Kohanski, D.J. Dwyer, J.J. Collins, How antibiotics kill bacteria: from targets to networks, Nat. Rev. Microbiol. 8 (6) (2010 Jun) 423–435.

[44] X. Lin, J. Song, X. Chen, H. Yang, Ultrasound-activated sensitizers and applications, Angew. Chem. Int. Ed. 59 (34) (2020).

[45] J. Qu, X. Zhao, P.X. Ma, B. Guo, Injectable antibacterial conductive hydrogels with dual response to an electric field and pH for localized "smart" drug release, Acta Biomater. 72 (2018) 55–69.

[46] C. Ghobril, M.W. Grinstaff, The chemistry and engineering of polymeric hydrogel adhesives for wound closure: a tutorial, Chem. Soc. Rev. 44 (7) (2015) 1820–1835.

[47] D. Gopinath, M.R. Ahmed, K. Gomathi, K. Chitra, P.K. Sehgal, R. Jayakumar, Dermal wound healing processes with curcumin incorporated collagen films, Biomaterials 25 (10) (2004) 1911–1917.

[48] C. Ghobril, M.W. Grinstaff, The chemistry and engineering of polymeric hydrogel adhesives for wound closure: a tutorial, Chem. Soc. Rev. 44 (7) (2015) 1820.

[49] J. Qu, X. Zhao, P.X. Ma, B. Guo, pH-responsive self-healing injectable hydrogel based on N-carboxyethyl chitosan for hepatocellular carcinoma therapy, Acta Biomater. (2017), S1742706117303537.

[50] R. Ross, The fibroblast and wound repair, Biol. Rev. 43 (1) (2010) 51–91.

[51] G.C. Gurtner, S. Werner, Y. Barrandon, M.T. Longaker, Wound repair and regeneration, Nature 453 (7193) (2008) 314–321.

[52] G. Wang, H. Feng, L. Hu, et al., An antibacterial platform based on capacitive carbon-doped TiO(2) nanotubes after direct or alternating current charging, Nat. Commun. 9 (1) (2018) 2055.

[53] Y. Zhang, Q. An, S. Zhang, et al., A healing promoting wound dressing with tailor-made antibacterial potency employing piezocatalytic processes in multi-functional nanocomposites, Nanoscale 14 (7) (2022) 2649–2659.

[54] B. Sda, B. Hs, X.A. Ge, et al., Self-powered and Photothermal Electronic Skin Patches for Accelerating Wound Healing, 2021.

[55] Y. Xiang, C. Mao, X. Liu, et al., Rapid and superior bacteria killing of carbon quantum dots/ZnO decorated injectable folic acid-conjugated PDA hydrogel through dual-light triggered ROS and membrane permeability, Small 15 (22) (2019), e1900322.

[56] B.C. Dickinson, C.J. Chang, Chemistry and biology of reactive oxygen species in signaling or stress responses, Nat. Chem. Biol. 7 (8) (2011) 504–511.

[57] Christopher, James Cowell, et al., Ultrasonic stimulation of mouse skin reverses the healing delays in diabetes and aging by activation of Rac1, J. Invest. Dermatol. 135 (11) (2015) 2842–2851.

[58] Y. Ishida, Y. Kuninaka, M. Nosaka, M. Furuta, T. Kondo, CCL2-Mediated reversal of impaired SkinWound healing in diabetic mice byNormalization of neovascularization and Collagen accumulation, J. Invest. Dermatol. 139 (12) (2019) 2517–2527, e5.

[59] Susan W. Volk, et al., Diminished type III collagen promotes myofibroblast differentiation and increases scar deposition in cutaneous wound healing, Cells Tissues Organs 194 (1) (2011) 25–37.

[60] G. Priya, T. Leslie, S. Snehal, M. James, P. Ellen, CD44-dependent inflammation, fibrogenesis, and collagenolysis regulates extracellular matrix remodeling and tensile strength during cutaneous wound healing, Matrix Biol. 75-76 (2018) 314–330. S0945053X18301276-.

[61] C. Liu, D. Chu, K. Kalantar-Zadeh, J. George, H.A. Young, G. Liu, Cytokines: from clinical significance to quantification, Adv. Sci. 8 (15) (2021), e2004433.

[62] M. Wang, C. Wang, M. Chen, Y. Xi, B. Lei, Efficient angiogenesis-based diabetic wound healing/skin reconstruction through bioactive antibacterial adhesive ultra-violet shielding nanodressing with exosome release, ACS Nano 13 (9) (2019).

[63] C. Chen, Y. Liu, H. Wang, et al., Multifunctional chitosan inverse opal particles for wound healing, ACS Nano 12 (10) (2018) 10493–10500.

[64] X. Zhang, G. Chen, Y. Liu, L. Sun, L. Sun, Y. Zhao, Black phosphorus-loaded separable microneedles as responsive oxygen delivery carriers for wound healing, ACS Nano 14 (5) (2020) 5901–5908.

[65] P. Lertkiatmongkol, D. Liao, H. Mei, Y. Hu, P.J. Newman, Endothelial functions of platelet/endothelial cell adhesion molecule-1 (CD31), Curr. Opin. Hematol. 23 (3) (2016) 1.

[66] C.G. Wang, Y.T. Lou, M.J. Tong, et al., Asperosaponin VI promotes angiogenesis and accelerates wound healing in rats via up-regulating HIF-1α/VEGF signaling, Acta Pharmacol. Sin. 39 (3) (2018) 393–404.